NANO LETTERS

pubs.acs.org/NanoLett Letter

Machine Learning-Enabled Superior Energy Storage in Ferroelectric Films with a Slush-Like Polar State

Ruihao Yuan, Abinash Kumar, Shihao Zhuang, Nicholas Cucciniello, Teng Lu, Deqing Xue, Aubrey Penn, Alessandro R. Mazza, Quanxi Jia, Yun Liu, Dezhen Xue,* Jinshan Li,* Jia-Mian Hu, James M. LeBeau, and Aiping Chen*

Cite This: *Nano Lett.* 2023, 23, 4807−4814 Read Online

ACCESS | Metrics & More | Article Recommendations | Supporting Information

ABSTRACT: Heterogeneities in structure and polarization have been employed to enhance the energy storage properties of ferroelectric films. The presence of nonpolar phases, however, weakens the net polarization. Here, we achieve a slush-like polar state with fine domains of different ferroelectric polar phases by narrowing the large combinatorial space of likely candidates using machine learning methods. The formation of the slush-like polar state at the nanoscale in cation-doped $BaTiO_3$ films is simulated by phase field simulation and confirmed by aberration-corrected scanning transmission electron microscopy. The large polarization and the delayed polarization saturation lead to greatly enhanced energy density of 80 J/cm^3 and transfer efficiency of 85% over a wide temperature range. Such a data-driven design recipe for a slush-like polar state is generally applicable to quickly optimize functionalities of ferroelectric materials.

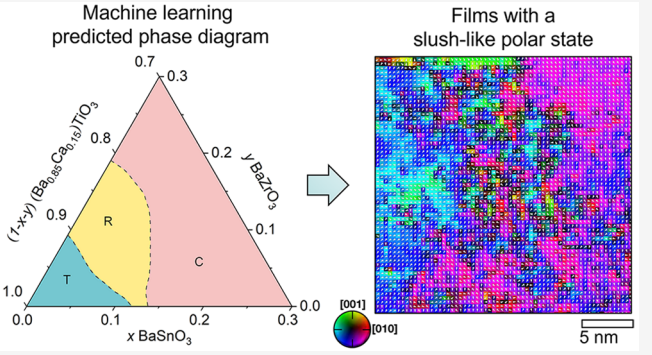

KEYWORDS: *ferroelectric films, machine learning, energy storage, slush-like polar state*

Downloaded via UNIV OF WISCONSIN-MADISON on June 27, 2023 at 17:34:06 (UTC).
See https://pubs.acs.org/sharingguidelines for options on how to legitimately share published articles.

Dielectric materials, holding charges as capacitors, are vital energy storage components of electronics and power systems.[1−3] In contrast to electrochemical energy storage techniques in fuel cells and batteries, dielectric capacitors distinguish themselves in features of ultrafast charging/discharging rates, high voltage endurance, and good reliability.[4−6] Enhancing the relatively low energy densities of dielectric capacitors is essential for applications such as pulsed power equipment, for which device miniaturization, system compactness, and cost reduction are required.[7−9] Therefore, considerable effort has been devoted to enhancing the energy storage via composition optimization, defect engineering, and architectural design.[10−12]

Two key parameters for energy storage in capacitors include the recoverable energy density W_{re} and the transfer efficiency η.[3] The former is determined by $W_{re} = \int_{P_r}^{P_{max}} E\,dP$, where E is the applied electric field, P_{max} is the maximum polarization, and P_r is the remnant polarization. The latter is defined as $\eta = \int_{P_r}^{P_{max}} E\,dP / \int_{0}^{P_{max}} E\,dP$. Accordingly, a large polarization (P_{max}) and a large difference between P_{max} and P_r ($P_{max} - P_r$) as well as a high breakdown strength (E_b) are favored to enhance both W_{re} and η.[3] The focus so far has been on introducing structural heterogeneities inside the materials.[13,14] Examples include the formation of relaxor ferroelectrics or superparaelectric states by chemical modification to suppress P_r,[15] the introduction of defects by ion-bombardment to delay the polarization saturation,[3] and the construction of specific interfaces and grain orientations to enhance E_b.[16]

Structural heterogeneities play a crucial role in relaxor ferroelectrics,[3,17,18] as polar nanoregions (PNRs) are embedded in a nonpolar matrix,[19] as shown in Figure 1A. The reduced domain size and the weak intercoupling between the PNRs lead to low domain switching energy barriers. This results in suppressed hysteresis with low energy dissipation.[20] Meanwhile, the sluggish response of the glass-like relaxor state to the external stimuli causes substantially delayed polarization saturation (P_{max} is not achieved until the field reaches E_b).[21] These aspects can be employed to improve both η and W_{re}. However, the presence of a nonpolar cubic phase weakens the net polarization (P_{max}), which can in turn result in decreasing W_{re} and η.[15,22] Retaining the PNRs while suppressing the nonpolar state is thus an effective strategy. Here, we achieve a

Received: January 23, 2023
Revised: May 18, 2023
Published: May 24, 2023

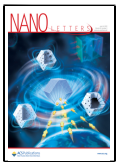

ACS Publications © 2023 American Chemical Society

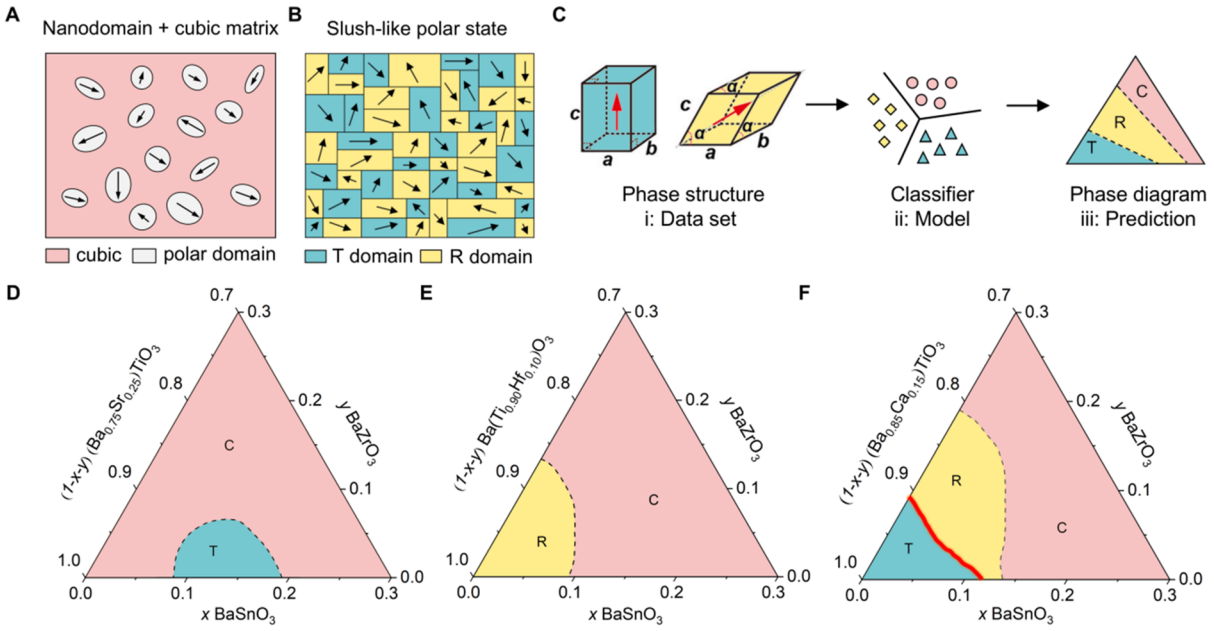

Figure 1. Design of a slush-like polar state to enhance energy storage performance via machine learning. (A) Polar nanoregions embedded in a nonpolar matrix. (B) A slush-like polar state with nanoscale domains. (C) Machine learning guided design strategy from data to prediction. Typical pseudoternary phase diagrams containing (D) cubic−tetragonal (C−T) phase boundary, (E) cubic−rhombohedral (C−R) phase boundary and (F) rhombohedral−tetragonal (R−T) phase boundary.

slush-like polar state[23,24] of multiple ferroelectric phases with small domains exhibiting low angle domain walls and high domain wall density, as schematically shown in Figure 1B. It contains nanoscale fluctuations of dipoles at the phase boundaries of differing ferroelectric phases. The state is associated with very low energy barriers across domains and nearly vanishing polarization anisotropy, thereby utilizing the contributions of PNRs without sacrificing the net polarization.

Machine Learning Guided Design of System with a Slush-Like Polar State. A lead-free model system of cation modified $BaTiO_3$ was selected to obtain a slush-like polar state, because of its good manufacturability, stability, and solubility with dopants.[25] The idea is to search for a system containing multiphase coexistence of different low symmetry phases. Such a multiphase coexistence state corresponds to very low energy barriers between different polar states. We herein aim to design compositions with rhombohedral−tetragonal (R−T) mixed phases, as they have been demonstrated to show significantly improved dielectric and piezoelectric properties due to the mostly flattened free energy surface, which might be promising for enhanced energy storage performance.[20,26] However, the obstacle lies in the vast search space of potential compositions, since various cations of Ca^{2+}, Sr^{2+}, Zr^{4+}, Hf^{4+}, and Sn^{4+} can potentially be substituted for Ba^{2+} and Ti^{4+} to form a variety of solid solutions: $(1-x-y)Ba_{1-w}Ca_wTiO_3-xBaZrO_3-yBaSnO_3$, $(1-x-y)Ba_{1-w}Sr_wTiO_3-xBaZrO_3-yBaSnO_3$, and $(1-x-y)BaTi_{1-w}Hf_wO_3-xBaZrO_3-yBaSnO_3$. By limiting the values of x, y, and w to the range of 0−0.3 with $x + y \leq 0.3$ and using the increment 0.01, approximately 140,000 unexplored compositions are possible. To efficiently explore this vast space, a machine learning guided strategy is employed (Figure 1C). Such a data-driven approach is increasingly being utilized in materials science to accelerate the design of new materials.[27−30] We built a supervised machine learning classification model to predict the phases of all the possible compositions and thereby to construct pseudoternary phase diagrams, each of which can contain different phase boundaries. The phase diagrams containing the R−T phase boundary are then rapidly identified to achieve our design target.

The initial data set used to train the machine learning surrogate model consists of 181 compositions of ceramics, which were synthesized and characterized in the same lab to reduce the uncertainties associated with the fabrication and measurements. Of these, 50 compositions are labeled "cubic" (C) and 76, "tetragonal" (T), while the remaining 55 are "rhombohedral" (R). The confusion matrix from the classification model indicates good model performance with an accuracy of 0.92 (Figure S1). The trained model then predicts the phase type of all the ∼140,000 possible compositions. Figure 1D−F gives three typical pseudoternary phase diagrams based on the predictions. The ones containing Sr^{2+} in Figure 1D and Hf^{4+} in Figure 1E possess C−T and C−R phase boundaries, respectively. These boundaries could facilitate the formation of the relaxor state due to the existence of the nonpolar cubic phase; however, they are beyond our interest of suppressing the nonpolar matrix. Thus, our focus is on the phase diagrams containing the R−T phase boundaries, and the one of $(1-x-y)Ba_{0.85}Ca_{0.15}TiO_3-xBaZrO_3-yBaSnO_3$ is shown as an example in Figure 1F. From the predicted ternary compositional phase diagrams, many compositions exist near the R−T phase boundary. As the predictions contain uncertainties and to select the most promising compositions as the target materials for thin film fabrication, we estimate the probability for each composition to be located at the R−T boundary, and the top ten with relatively large probabilities are listed in Table S1. Accordingly, we selected three compositions, i.e., $0.90Ba_{0.82}Ca_{0.18}TiO_3-0.09BaZrO_3-0.01BaSnO_3$ (1Sn), $0.90Ba_{0.82}Ca_{0.18}TiO_3-0.07BaZrO_3-0.03BaSnO_3$ (3Sn), and $0.90Ba_{0.82}Ca_{0.18}TiO_3-0.05BaZrO_3-0.05BaSnO_3$ (5Sn), in which the B-site Sn^{4+} concentration changes monotonically to further tolerate the uncertainties between the ceramics and films. For comparison, we also synthesized

https://doi.org/10.1021/acs.nanolett.3c00277
Nano Lett. 2023, 23, 4807−4814

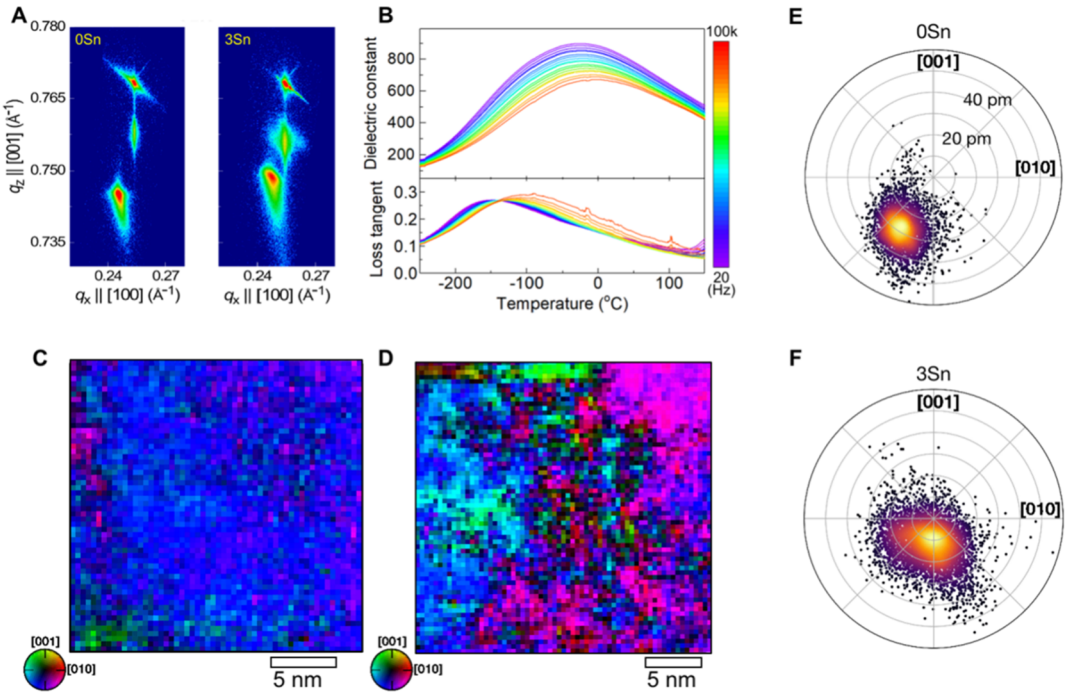

Figure 2. Indication of the slush-like polar state. (A) The RSM result for the 0Sn and 3Sn thin films. (B) The temperature dependence of the dielectric constant and loss tangent of the 3Sn thin film. The projected displacement (polarization) map for 0Sn (C) and 3Sn (D) thin films. The projected displacement magnitude ranges from 0 to 33 pm for the 0Sn map and 0 to 22 pm for the 3Sn map, as indicated by luminosity. Polar plots of unit cell polarization vectors for 0Sn (E) and 3Sn (F) samples.

the well-known lead-free system of $0.50Ba_{0.70}Ca_{0.30}TiO_3-0.50BaTi_{0.80}Zr_{0.20}O_3$ (0Sn)[26] with R and T phase coexistence. It should be noted that our machine learning assisted composition screening is based on the bulk data, as it is easier to construct a relatively large data set of ceramics of different compositions with characterized phase structures. It is also reported that there may be an intermediate orthorhombic (O) phase between the R and T phase boundary.[31] We only consider the R−T boundary for simplicity. The films synthesized using a nonequilibrium pulsed laser deposition may lead to some differences in stoichiometry due to varying vapor pressure of different oxides. However, the construction of a data set of films with different compositions and phase structures is much more expensive and time intensive.

Multiscale Characterization of a Slush-Like Polar State. High quality epitaxial thin films of 0Sn, 1Sn, 3Sn, and 5Sn were deposited on the $SrRuO_3$ (SRO) buffered $SrTiO_3$ (001) substrates by pulsed laser deposition. The detailed growth procedure is depicted in the Supporting Information. Top electrodes were deposited by magnetron sputtering via a shadow mask. The actual size of the top electrodes was estimated by scanning electron microscopy (Figure S2). The film quality has been investigated by thin film X-ray diffraction and scanning transmission electron microscopy (STEM). The cross-sectional annular dark-field (ADF) STEM images for the 0Sn and 3Sn films in Figure S3 show a sharp interface formed between the film and SRO buffer layer and SRO and the substrate, indicating the excellent epitaxial quality. Energy-dispersive X-ray spectroscopy (EDS) in STEM reveals (Figure S4) evidence of uniform cation distributions across the film thickness and no phase separation, due to the high solubility of Ca, Zr, and Sn in $BaTiO_3$. According to EDS data, the composition of the 3Sn film is determined to be $Ba_{0.84}Ca_{0.16}Ti_{0.88}Zr_{0.09}Sn_{0.03}O_3$, which is close to the target composition. This indicates that there is no strong stoichiometry deviation for the film growth of this five-cation compound. Figure 2A shows the STO (103) reciprocal space mapping (RSM) results for the 0Sn and 3Sn thin films. The 100 nm SRO bottom electrode layer is strained to the STO substrate, while the 0Sn and 3Sn thin film (~270 nm) layers are fully relaxed. The elongated RSM peaks may indicate the coexistence of R and T phases.[20] To confirm the phase, the RSMs of 103, 013, $\bar{1}03$, and $0\bar{1}3$ reflections for 0Sn and 3Sn films were performed (Figure S5). The comparison of these results indicates the existence of the orthorhombic (O) phase.[32] We can not exclude the existence of the R phase. It should be noted that the O phase is the intermediate phase between the R and T phase boundary. It was reported that the T−O phase boundary is lower than that at the O−R phase boundary and the coexistence of R−O−T reduces energy barriers and facilitates polarization rotation.[33,34] It is interesting that the thin film technique promotes the growth of the O phase. For 0Sn films (O phase), the lattice parameters are a = 4.020 Å, b = 4.027 Å, and c = 4.016 Å, while the lattice parameters of the 3Sn films (O phase) are smaller with a = 4.008 Å, b = 4.022 Å, and c = 4.011 Å (Table S2). The larger lattice parameters for the 0Sn samples compared to bulk materials with the same composition (a = b = 3.999 Å, c = 4.009 Å)[35] could be due to the formation of oxygen vacancy in the films. It was often reported that oxygen vacancy enlarges lattice parameter and volume.[36] Therefore, the reducing lattice parameters with Sn doping indicates less oxygen vacancies formed in the Sn-doped films. This is consistent with the breakdown field enhancement discussed later.

The phase coexistence and relaxor behavior was then investigated by measuring the dielectric constant (ε)/loss tangent (tanδ) spectrum. Figure 2B shows the temperature dependence of ε and tanδ for the 3Sn film, under different

https://doi.org/10.1021/acs.nanolett.3c00277
Nano Lett. 2023, 23, 4807−4814

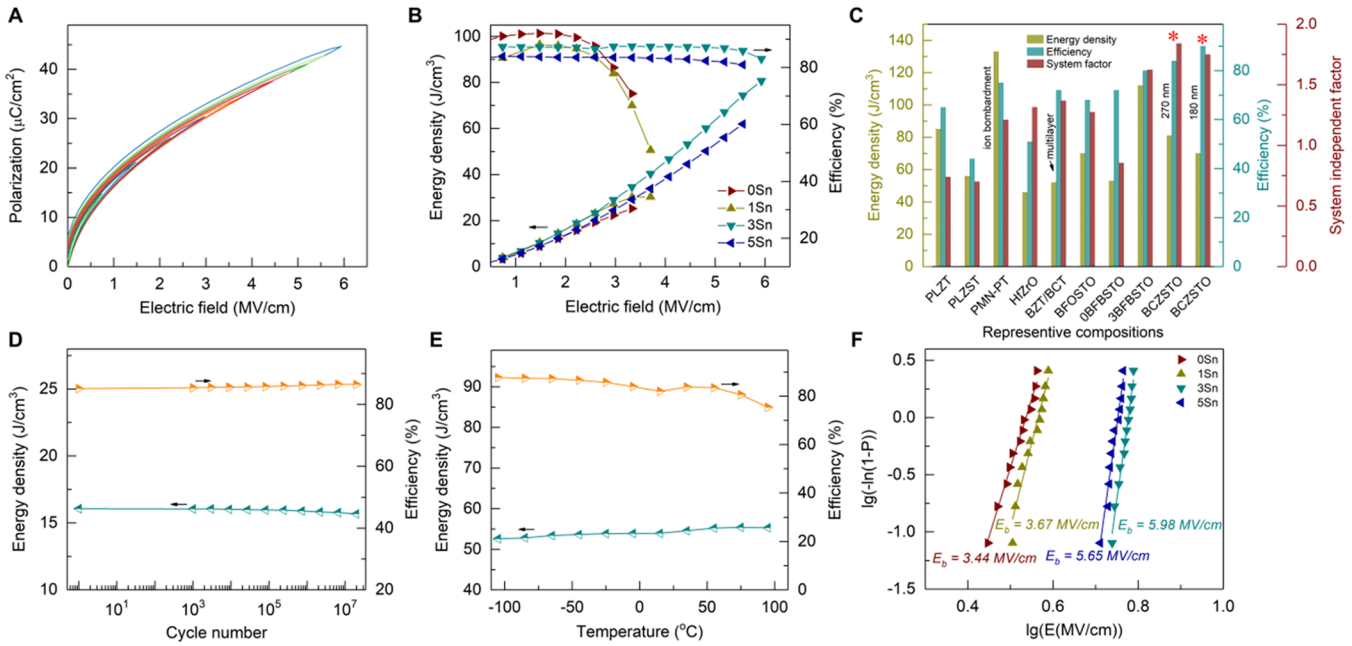

Figure 3. Energy storage performance of the $BaTiO_3$-based films. (A) The P–E loops for the 3Sn film. (B) The energy density and transfer efficiency as a function of electric filed for 0Sn, 1Sn, 3Sn, and 5Sn thin films. (C) The best performer in this study in comparison to the state-of-the-art reported for lead-based and lead-free thin films. (D) The energy density and transfer efficiency as a function of the cycle number. (E) The temperature stability of energy density and transfer efficiency. (F) Weibull distribution to evaluate the dielectric stability of the synthesized films.

frequencies changing from 20 Hz to 100 kHz. The shift in the dielectric constant and loss tangent peaks suggest a strong relaxation behavior. The dielectric result for the 0Sn film is shown in Figure S6 as a comparison. We then confirmed the slush-like polar state at the atomic scale using integrated differential phase contrast (iDPC) STEM imaging, which provides the projected positions of both cation and anion sublattices. The projected net displacement (polarization) is measured as the difference between the centroids for atom columns cations/cations-oxygen and the pure oxygen anions in the films of 0Sn and 3Sn. Figure 2C,D shows representative projected polarization maps for 0Sn and 3Sn imaged along ⟨001⟩, respectively. In these polar maps, the variation in polarization vectors in terms of their direction and magnitude are indicated by different colors and luminosity, respectively. The varying color and luminosity in polar maps for both samples indicate a lack of long-range ordering, different from normal ferroelectric thin films. In addition, the observed polar domains do not decay to a nonpolar state. This means the domain structure in our samples are different from the polar nanoregion model (polar domains in nonpolar matrix). Our results indicate that both 0Sn and 3Sn samples exhibit a slush-like polar state. With Sn doping (Figure 2D), the domain size reduces significantly. The presence of nanoscale polar domains with low-angle and high-density domain walls are shown in maps with arrows (Figure S7). The nanoscale domains in 3Sn vary in size from 2 to 10 nm, while 0Sn shows a larger domain size. To quantify the polarization vector distribution, we performed more analysis on Figure S7. Figure 2E,F shows polar plots of unit cell polarization vectors for 0Sn and 3Sn samples. The polarization vector distribution angle (~120°) of the 3Sn sample is much wider than that (~50°) of the 0Sn sample for the same sampling area, indicating a vanishing polarization anisotropy in the 3Sn sample. Due to such small domain size and weakened polarization anisotropy, the polarization of nanodomains can thus flip among energy equivalent directions easily in the 3Sn thin films, which could render a high energy storage response. Therefore, we observed high density nanoscale polar domains in Zr/Ca-codoped BTO films and Sn doping further increase the density of nano-domains by reducing the size. The above results confirmed a slush-like polar state in our doped BTO films.

Superior Energy Storage Properties of the Slush-Like Polar State. Figure 3A represents the unipolar polarization–electric field (P–E) curves for the 3Sn film. The narrow P–E curves are characteristic of relaxor ferroelectrics. Those for 0Sn, 1Sn, and 5Sn are shown in Figure S8, which are quite different from the square loops of their bulk counterparts (Figure S9). The energy density W_{re} and transfer efficiency η of the Sn-doped films under different fields are calculated by integrating the unipolar P–E curves, as shown in Figure 3B, where the W_{re} and η for 0Sn are also included as a comparison. The W_{re} of 3Sn and 5Sn films outperforms that of 0Sn and 1Sn films. The W_{re} for 3Sn and 5Sn films reaches ~80 J/cm^3 at 5.9 MV/cm and ~62 J/cm^3 at 5.5 MV/cm, respectively. The efficiency η for 3Sn and 5Sn films keep almost a constant value of ~85% even approaching E_b. Note that the η values for 0Sn and 1Sn films are comparable to those of 3Sn and 5Sn films at low fields but dramatically decrease with the increasing electric field above 3 MV/cm. We compare the best performer synthesized in the present study to other lead-based and lead-free films that have been reported, as shown in Figure 3C. The 3Sn thin film shows excellent η (~85%), superior to the state-of-the-art systems. The W_{re} (80 J/cm^3) is larger than most reports, including the BZT/BCT multilayer in which normal ferroelectric polar state appears.[25] Therefore, the construction of the slush-like polar state can be an effective way to improve the energy storage performance of ferroelectric thin films. However, it is still lower than recent reports of ion-bombardment enhanced lead-based PMN–PT[3] and composition optimized lead-free $BiFeO_3$ systems.[20] This is not surprising as the W_{re} is proportional to the maximum

https://doi.org/10.1021/acs.nanolett.3c00277
Nano Lett. 2023, 23, 4807–4814

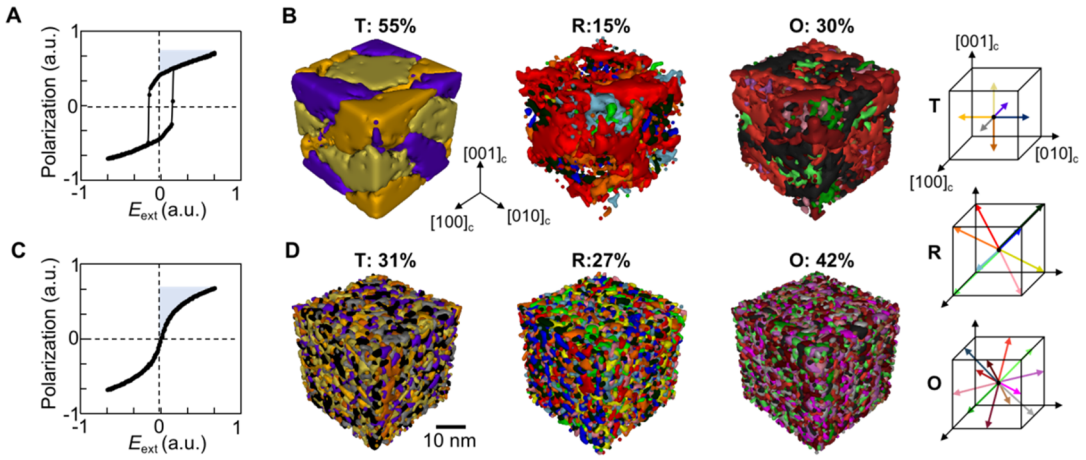

Figure 4. Phase field simulation of the slush-like polar state. (A) The simulated ferroelectric hysteresis loop of (001) 0Sn film with long-range domains and (B) 3D morphology of T, R, and O components of the polarization domains at zero field. (C) The simulated $P-E$ loop of (001) 3Sn film with ultrafine-scale nanodomains and (D) the corresponding 3D morphology of T, R, and O components of the polarization domains at zero field. In (B) and (D), the different colors represent different directions of the local polarization vectors, with the corresponding color code shown in the rightmost column. Volume fractions of T, R, and O domains are indicated. Scale bar is 10 nm.

polarization, which is strongly dielectric system dependent. For example, the spontaneous polarizations of $PbTiO_3$, $BiFeO_3$, and $BaTiO_3$ are ~80, ~80, and ~25 $\mu C/cm^2$, respectively. The corresponding W_{re} values are 135 J/cm^3 in ion-bombardment enhanced lead-based PMN−PT,[3] 110 J/cm^3 in composition optimized lead-free $BiFeO_3$,[20] and 80 J/cm^3 in our $BaTiO_3$-based systems. To compare fairly across different dielectric systems, we define a system independent figure of merit f, which is given by $f = W_{re}/P_{max}$. In this context, the f values for PMN−PT and $BiFeO_3$-based thin film are about 1.2 and 1.3, respectively. In contrast, the f values for our 3Sn (270 nm) and 5Sn (180 nm) films are ~1.85 and ~1.75, about 50% higher than those of the former two. This may hint that the application of the slush-like polar state can further optimize the energy storage performance of Pb-based and $BiFeO_3$-based systems that have high spontaneous polarization.

To characterize the fatigue performance of the synthesized films, a cycling test under a triangle field of 2.5 MV/cm and 10 kHz is conducted for the 3Sn film. Figure 3D shows the W_{re} and η as a function of the cycle number. Both parameters are stable even after the cycling number reaches a high value of 10^7, indicating an excellent fatigue resistance. The exploration of the origin of fatigue has always been a long-term challenge and is still under debate; even various models such as local phase decomposition and domain wall pinning have been proposed.[37−39] In our case, the robust cycle reliability might be ascribed to the Sn doping induced oxygen vacancy concentration reduction.[39] The temperature stability of the energy storage performance serves as an important figure of merit for practical applications of dielectric capacitors. Figure 3E plots W_{re} and η as a function of temperature that changes in a large range from −110 to 100 °C. Both W_{re} and η show slight temperature dependence, ensuring the operation in a wide temperature window. Specifically, W_{re} is higher than 50 J/cm^3 and increases slightly with the increasing temperature. η shows a high value of ~85% from −110 to 60 °C, and it decreases at elevated temperatures (~77% at 100 °C). This stability of η can be understood from the similar leakage current behavior at −100 and 25 °C (Figure S10). The power law dependent current−voltage behavior indicates the space charge limited conduction mechanism.[40] At 100 °C, thermal energy activates carriers associated with deep traps, which results in higher leakage current and lower η. It makes the $P-E$ curves fatter (Figure S11) and subsequently decreases the energy transfer efficiency, as presented in Figure 3E.

The results above indicate that E_b plays an important role in enhancing the energy storage performance. We thus analyze the E_b of the fabricated films using a two-parameter Weibull distribution linear fitting, as shown in Figure 3F. The E_b values for 3Sn and 5Sn are higher than 5.5 MV/cm. This E_b is comparable to the state-of-the-art results in ferroelectric oxide thin films.[3,20] The slope of the fitting line, r, represents the dielectric stability under multiple measurements. We see that the r for 3Sn and 5Sn is higher than the other two, indicating good uniformity and stability. To understand the origin of the enhanced E_b and energy storage performance in 3Sn thin films, we conducted electron energy loss spectroscopy (EELS) analysis to characterize the valence state of the Ti cations with different Sn contents. The valence state of Ti in 0Sn and 3Sn films, as compared to a standard $SrTiO_3$, is shown in Figure S12. Ti L_2 and L_3 edges of 3Sn film match better with the standard $SrTiO_3$ while those of the 0Sn film have a lower energy onset, indicating the presence of Ti^{3+} and oxygen vacancy.[41] In other words, Sn doping reduces the presence of Ti^{3+} and oxygen vacancy, which is consistent with RSM results. Thus, we conclude that Sn doping reduces oxygen vacancy concentration, decreases lattice parameters, and enhances the dielectric properties such as fatigue and E_b. Therefore, the enhancement of energy storage performance can be attributed to the presence of small multiphase domains together with the stabilization of Ti^{4+}.

Domain Size Effect of the Slush-Like Polar State. Phase-field simulations were performed to simulate the effects of ultrasmall multiphase ferroelectric domains on the polarization switching behavior in such a solid solution film. All input parameters of the model were taken from reported values, except that the gradient energy coefficient that is proportional to domain wall energy is tuned to change the domain size and domain wall density. In the case of a large gradient energy coefficient, the film displays a hysteresis loop with a relatively large coercive field (Figure 4A), along with a mixture of T, R, and O domains at zero electric field (Figure

https://doi.org/10.1021/acs.nanolett.3c00277
Nano Lett. 2023, 23, 4807−4814

4B). The size of these ferroelectric domains is relatively large with long-range ordering, and the volumetric fraction of the T domains (~55%) is dominant, which gives rise to relatively large remanent polarization as shown in Figure 4A. With decreasing gradient energy coefficient, the film shows multiple phases coexist (T, R, and O phases) at zero field but the domain size is much smaller without long-range ordering, as shown in Figure 4D. These ultrafine-scale nanodomains lead to a slim $P-E$ loop with negligible hysteresis, very low coercive field, and almost zero remanent polarization (Figure 4C), as in typical relaxor ferroelectric systems. The state exhibits very low energy barrier and nearly vanishing polarization anisotropy and thereby utilizes the contributions of PNRs without sacrificing the net polarization.

We have demonstrated that a slush-like polar state suppressing the nonpolar matrix exhibits superior energy storage density and transfer efficiency. Such a state is not limited to $BaTiO_3$-based systems but applicable to other energy storage dielectrics. It also benefits other functionalities that require minimized hysteresis and large polarization. The efficient searching strategy with the assistance of machine learning can be generalized to other multiphase functional materials.

■ ASSOCIATED CONTENT

Supporting Information

The Supporting Information is available free of charge at https://pubs.acs.org/doi/10.1021/acs.nanolett.3c00277.

Experimental section/methods details on the film growth, STEM characterization, machine learning, and phase field simulation; confusion matrix of the classification model based on machine learning; the top ten compositions with high probability to be located on the R−T boundary; Top electrodes measured by Scanning Electron Microscope; ADF STEM images of cross-section of 0Sn and 3Sn thin films; STEM-EDS elemental maps for 3Sn thin film; in-plane and out-of-plane lattice parameters comparison; lattice parameters for 0Sn and 3Sn thin films; the temperature dependence of dielectric constant and loss tangent for the 0Sn thin film; projected displacement (polarization) map for 0Sn and 3Sn films; polarization vs electric field curves for 0Sn, 1Sn, and 5Sn films; $P-E$ loops for bulk ceramics of 0Sn, 1Sn, 3Sn, and 5Sn; leakage current as a function of electric field at different temperatures for 3Sn film; $P-E$ curves at temperatures ranging from −105 to 95 °C for 3Sn thin film; electron energy loss spectrum for 0Sn and 3Sn films (PDF)

■ AUTHOR INFORMATION

Corresponding Authors

Dezhen Xue − *State Key Laboratory for Mechanical Behavior of Materials, Xi'an Jiaotong University, Xi'an 710049, China*; Email: xuedezhen@xjtu.edu.cn

Jinshan Li − *State Key Laboratory of Solidification Processing, Northwestern Polytechnical University, Xi'an 710072, China*; Email: ljsh@nwpu.edu.cn

Aiping Chen − *Center for Integrated Nanotechnologies (CINT), Los Alamos National Laboratory, Los Alamos, New Mexico 87545, United States*; orcid.org/0000-0003-2639-2797; Email: apchen@lanl.gov

Authors

Ruihao Yuan − *T-4, Los Alamos National Laboratory, Los Alamos, New Mexico 87545, United States; State Key Laboratory of Solidification Processing, Northwestern Polytechnical University, Xi'an 710072, China*

Abinash Kumar − *Department of Materials Science and Engineering, Massachusetts Institute of Technology, Cambridge, Massachusetts 02139, United States*

Shihao Zhuang − *Department of Materials Science and Engineering, University of Wisconsin-Madison, Madison, Wisconsin 53706, United States*

Nicholas Cucciniello − *Center for Integrated Nanotechnologies (CINT), Los Alamos National Laboratory, Los Alamos, New Mexico 87545, United States; Department of Materials Design and Innovation, University at Buffalo-The State University of New York, Buffalo, New York 14260, United States*; orcid.org/0000-0002-9399-4985

Teng Lu − *Research School of Chemistry, The Australian National University, Canberra, Australian Capital Territory 2601, Australia*; orcid.org/0000-0002-7866-1859

Deqing Xue − *State Key Laboratory for Mechanical Behavior of Materials, Xi'an Jiaotong University, Xi'an 710049, China*

Aubrey Penn − *MIT.nano, Massachusetts Institute of Technology, Cambridge, Massachusetts 02139, United States*; orcid.org/0000-0001-7586-1655

Alessandro R. Mazza − *Center for Integrated Nanotechnologies (CINT), Los Alamos National Laboratory, Los Alamos, New Mexico 87545, United States*

Quanxi Jia − *Department of Materials Design and Innovation, University at Buffalo-The State University of New York, Buffalo, New York 14260, United States*

Yun Liu − *Research School of Chemistry, The Australian National University, Canberra, Australian Capital Territory 2601, Australia*; orcid.org/0000-0002-5404-3909

Jia-Mian Hu − *Department of Materials Science and Engineering, University of Wisconsin-Madison, Madison, Wisconsin 53706, United States*; orcid.org/0000-0002-7579-6440

James M. LeBeau − *Department of Materials Science and Engineering, Massachusetts Institute of Technology, Cambridge, Massachusetts 02139, United States*; orcid.org/0000-0002-7726-3533

Complete contact information is available at: https://pubs.acs.org/10.1021/acs.nanolett.3c00277

Author Contributions

R.H.Y., D.Z.X., and A.P.C. conceived this study. R.H.Y. and A.P.C. fabricated the films and measured the ferroelectric property and energy storage performance. R.H.Y. built the machine learning model with the supervision of D.Z.X. and J.S.L. Y.L. and T.L. conducted the dielectric constant measurement. A.K., A.P., and J.M.L. performed the STEM characterization. D.Q.X. characterized microstructure of some samples by STEM. S.H.Z. performed the phase-field simulations under the supervision of J.-M.H. N.C., A.R.M., Q.X.J., and A.P.C. conducted the RSM measurements and data analysis. R.H.Y., D.Z.X. and A.P.C. wrote the first draft of the manuscript. All authors discussed the results and edited the manuscript.

Notes

The authors declare no competing financial interest.

https://doi.org/10.1021/acs.nanolett.3c00277
Nano Lett. 2023, 23, 4807−4814

■ ACKNOWLEDGMENTS

The work at Los Alamos National Laboratory was performed, in part, at the Center for Integrated Nanotechnologies, an Office of Science User Facility operated for the U.S. Department of Energy Office of Science. Los Alamos National Laboratory, an affirmative action equal opportunity employer, is managed by Triad National Security, LLC for the U.S. Department of Energy's NNSA, under contract 89233218CNA000001. R.H.Y. acknowledges the CINT user program for thin film synthesis and characterization. R.H.Y. and D.Z.X acknowledge the support of National Key Research and Development Program of China (2021YFB3802102) for the machine learning effort. A.P.C. thanks Prof. Joshua Agar for the discussion of machine learning. This work was carried out in part through the use of MIT.nano's facilities and in part at the Analytical Instrumentation Facility (AIF) at North Carolina State University, which is supported by the State of North Carolina and the National Science Foundation (award number ECCS-2025064). The AIF is a member of the North Carolina Research Triangle Nanotechnology Network (RTNN), a site in the National Nanotechnology Coordinated Infrastructure (NNCI). J.M.L. and A.K. acknowledge support of this work through the John Chipman Career Development Professorship. J.-M.H. acknowledges support from the National Science Foundation (NSF) Award No. CBET-2006028. The phase-field simulations were performed using Bridges at the Pittsburgh Supercomputing Center through Allocation No. TG-DMR180076, which is part of the Extreme Science and Engineering Discovery Environment and supported by NSF Grant No. ACI-1548562.

■ REFERENCES

(1) Chu, B. J.; Zhou, X.; Ren, K. L.; Neese, B.; Lin, M. R.; Wang, Q.; Bauer, F.; Zhang, Q. M. A dielectric polymer with high electric energy density and fast discharge speed. *Science* **2006**, *313*, 334−336.

(2) Li, Q.; Chen, L.; Gadinski, M. R.; Zhang, S. H.; Zhang, G. Z.; Li, H. Y.; Haque, A.; Chen, L. Q.; Jackson, T. N.; Wang, Q. Flexible high-temperature dielectric materials from polymer nanocomposites. *Nature* **2015**, *523*, 576−579.

(3) Kim, J.; Saremi, S.; Acharya, M.; Velarde, G.; Parsonnet, E.; Donahue, P.; Qualls, A.; Garcia, D.; Martin, L. W. Ultrahigh capacitive energy density in ion-bombarded relaxor ferroelectric films. *Science* **2020**, *369*, 81−84.

(4) Silva, J. P. B.; Sekhar, K. C.; Pan, H.; MacManus-Driscoll, J. L.; Pereira, M. Advances in Dielectric Thin Films for Energy Storage Applications, Revealing the Promise of Group IV Binary Oxides. *ACS Energy Lett.* **2021**, *6*, 2208−2217.

(5) Hao, Y.; Wang, X.; Bi, K.; Zhang, J.; Huang, Y.; Zhao, P.; Xu, K.; Lei, M.; Li, L. Significantly enhanced energy storage performance promoted by ultimate sized ferroelectric BaTiO3 fillers in nanocomposite films. *Nano Energy* **2017**, *31*, 49−56.

(6) Pan, Z.; Yao, L.; Zhai, J.; Yao, X.; Chen, H. Interfacial Coupling Effect in Organic/Inorganic Nanocomposites with High Energy Density. *Adv. Mater.* **2018**, *30*, 1705662.

(7) Prateek; Thakur, V. K.; Gupta, R. K. Recent Progress on Ferroelectric Polymer-Based Nanocomposites for High Energy Density Capacitors: Synthesis, Dielectric Properties, and Future Aspects. *Chem. Rev.* **2016**, *116*, 4260−4317.

(8) Xu, B.; Íñiguez, J.; Bellaiche, L. Designing lead-free antiferroelectrics for energy storage. *Nat. Commun.* **2017**, *8*, 15682.

(9) Yang, L.; Kong, X.; Li, F.; Hao, H.; Cheng, Z.; Liu, H.; Li, J.-F.; Zhang, S. Perovskite lead-free dielectrics for energy storage applications. *Prog. Mater. Sci.* **2019**, *102*, 72−108.

(10) Wang, G.; Li, J. L.; Zhang, X.; Fan, Z. M.; Yang, F.; Feteira, A.; Zhou, D.; Sinclair, D. C.; Ma, T.; Tan, X. L.; et al. Ultrahigh energy storage density lead-free multilayers by controlled electrical homogeneity. *Energy Environ. Sci.* **2019**, *12*, 582−588.

(11) Zhao, P. Y.; Wang, H. X.; Wu, L. W.; Chen, L. L.; Cai, Z. M.; Li, L. T.; Wang, X. H. High-Performance Relaxor Ferroelectric Materials for Energy Storage Applications. *Adv. Energy Mater.* **2019**, *9*, 1803048.

(12) Wang, K.; Ouyang, J.; Wuttig, M.; Zhao, Y. Y.; Cheng, H. B.; Zhang, Y.; Su, R. X.; Yan, J.; Zhong, X. L.; Zeng, F. Superparaelectric $(Ba_{0.95},Sr_{0.05})(Zr_{0.2},Ti_{0.8})O_3$ Ultracapacitors. *Adv. Energy Mater.* **2020**, *10*, 2001778.

(13) Shen, Z. H.; Wang, J. J.; Lin, Y. H.; Nan, C. W.; Chen, L. Q.; Shen, Y. High-Throughput Phase-Field Design of High-Energy-Density Polymer Nanocomposites. *Adv. Mater.* **2018**, *30*, 1704380.

(14) Zhang, T. D.; Li, W. L.; Zhao, Y.; Yu, Y.; Fei, W. D. High Energy Storage Performance of Opposite Double-Heterojunction Ferroelectricity-Insulators. *Adv. Funct. Mater.* **2018**, *28*, 1706211.

(15) Pan, H.; Lan, S.; Xu, S. Q.; Zhang, Q. H.; Yao, H. B.; Liu, Y. Q.; Meng, F. Q.; Guo, E. J.; Gu, L.; Yi, D.; et al. Ultrahigh energy storage in superparaelectric relaxor ferroelectrics. *Science* **2021**, *374*, 100−104.

(16) Li, J. L.; Shen, Z. H.; Chen, X. H.; Yang, S.; Zhou, W. L.; Wang, M. W.; Wang, L. H.; Kou, Q. W.; Liu, Y. C.; Li, Q.; et al. Grain-orientation-engineered multilayer ceramic capacitors for energy storage applications. *Nat. Mater.* **2020**, *19*, 999−1005.

(17) Cheng, H. B.; Ouyang, J.; Zhang, Y. X.; Ascienzo, D.; Li, Y.; Zhao, Y. Y.; Ren, Y. H. Demonstration of ultra-high recyclable energy densities in domain-engineered ferroelectric films. *Nat. Commun.* **2017**, *8*, 1999.

(18) Hu, Q. Y.; Tian, Y.; Zhu, Q. S.; Bian, J. H.; Jin, L.; Du, H. L.; Alikin, D. O.; Shur, V. Y.; Feng, Y. J.; Xu, Z.; et al. Achieve ultrahigh energy storage performance in $BaTiO_3$-$Bi(Mg_{1/2}Ti_{1/2})O_3$ relaxor ferroelectric ceramics via nano-scale polarization mismatch and reconstruction. *Nano Energy* **2020**, *67*, 104264.

(19) Bokov, A. A.; Ye, Z. G. Recent progress in relaxor ferroelectrics with perovskite structure. *J. Mater. Sci.* **2006**, *41*, 31−52.

(20) Pan, H.; Li, F.; Liu, Y.; Zhang, Q. H.; Wang, M.; Lan, S.; Zheng, Y. P.; Ma, J.; Gu, L.; Shen, Y.; et al. Ultrahigh-energy density lead-free dielectric films via polymorphic nanodomain design. *Science* **2019**, *365*, 578−582.

(21) Li, F.; Zhang, S. J.; Damjanovic, D.; Chen, L. Q.; Shrout, T. R. Local Structural Heterogeneity and Electromechanical Responses of Ferroelectrics: Learning from Relaxor Ferroelectrics. *Adv. Funct. Mater.* **2018**, *28*, 1801504.

(22) Pan, H.; Ma, J.; Ma, J.; Zhang, Q. H.; Liu, X. Z.; Guan, B.; Gu, L.; Zhang, X.; Zhang, Y. J.; Li, L. L.; et al. Giant energy density and high efficiency achieved in bismuth ferrite-based film capacitors via domain engineering. *Nat. Commun.* **2018**, *9*, 1813.

(23) Kumar, A.; Baker, J. N.; Bowes, P. C.; Cabral, M. J.; Zhang, S. J.; Dickey, E. C.; Irving, D. L.; LeBeau, J. M. Atomic-resolution electron microscopy of nanoscale local structure in lead-based relaxor ferroelectrics. *Nat. Mater.* **2021**, *20*, 62−67.

(24) Takenaka, H.; Grinberg, I.; Liu, S.; Rappe, A. M. Slush-like polar structures in single-crystal relaxors. *Nature* **2017**, *546*, 391−395.

(25) Sun, Z. X.; Ma, C. R.; Liu, M.; Cui, J.; Lu, L.; Lu, J. B.; Lou, X. J.; Jin, L.; Wang, H.; Jia, C. L. Ultrahigh Energy Storage Performance of Lead-Free Oxide Multilayer Film Capacitors via Interface Engineering. *Adv. Mater.* **2017**, *29*, 1604427.

(26) Liu, W. F.; Ren, X. B. Large Piezoelectric Effect in Pb-Free Ceramics. *Phys. Rev. Lett.* **2009**, *103*, 257602.

(27) Morgan, D.; Jacobs, R. Opportunities and Challenges for Machine Learning in Materials Science. *Annu. Rev. Mater. Res.* **2020**, *50*, 71−103.

(28) Butler, K. T.; Davies, D. W.; Cartwright, H.; Isayev, O.; Walsh, A. Machine learning for molecular and materials science. *Nature* **2018**, *559*, 547−555.

(29) Lookman, T.; Balachandran, P. V.; Xue, D. Z.; Yuan, R. H. Active learning in materials science with emphasis on adaptive sampling using uncertainties for targeted design. *npj Comput. Mater.* **2019**, *5*, 21.

https://doi.org/10.1021/acs.nanolett.3c00277
Nano Lett. 2023, 23, 4807−4814

(30) Yuan, R. H.; Liu, Z.; Balachandran, P. V.; Xue, D. Q.; Zhou, Y. M.; Ding, X. D.; Sun, J.; Xue, D. Z.; Lookman, T. Accelerated Discovery of Large Electrostrains in $BaTiO_3$-Based Piezoelectrics Using Active Learning. *Adv. Mater.* **2018**, *30*, 1702884.
(31) Acosta, M.; Novak, N.; Jo, W.; Rödel, J. Relationship between electromechanical properties and phase diagram in the Ba(Zr0.2Ti0.8)O3−x(Ba0.7Ca0.3)TiO3 lead-free piezoceramic. *Acta Mater.* **2014**, *80*, 48−55.
(32) Saito, K.; Ulyanenkov, A.; Grossmann, V.; Ress, H.; Bruegemann, L.; Ohta, H.; Kurosawa, T.; Ueki, S.; Funakubo, H. Structural Characterization of BiFeO3 Thin Films by Reciprocal Space Mapping. *Jpn. J. Appl. Phys.* **2006**, *45*, 7311.
(33) Yang, T.; Ke, X.; Wang, Y. Mechanisms Responsible for the Large Piezoelectricity at the Tetragonal-Orthorhombic Phase Boundary of (1-x)BaZr0.2Ti0.8O3-xBa0.7Ca0.3TiO3 System. *Sci. Rep.* **2016**, *6*, 33392.
(34) Zhao, C.; Wu, H.; Li, F.; Cai, Y.; Zhang, Y.; Song, D.; Wu, J.; Lyu, X.; Yin, J.; Xiao, D.; et al. Practical High Piezoelectricity in Barium Titanate Ceramics Utilizing Multiphase Convergence with Broad Structural Flexibility. *J. Am. Chem. Soc.* **2018**, *140*, 15252−15260.
(35) Coondoo, I.; Panwar, N.; Alikin, D.; Bdikin, I.; Islam, S. S.; Turygin, A.; Shur, V. Y.; Kholkin, A. L. A comparative study of structural and electrical properties in lead-free BCZT ceramics: Influence of the synthesis method. *Acta Mater.* **2018**, *155*, 331−342.
(36) Enriquez, E.; Chen, A.; Harrell, Z.; Dowden, P.; Koskelo, N.; Roback, J.; Janoschek, M.; Chen, C.; Jia, Q. Oxygen Vacancy-Tuned Physical Properties in Perovskite Thin Films with Multiple B-site Valance States. *Sci. Rep.* **2017**, *7*, 46184.
(37) Yang, S. M.; Kim, T. H.; Yoon, J. G.; Noh, T. W. Nanoscale Observation of Time-Dependent Domain Wall Pinning as the Origin of Polarization Fatigue. *Adv. Funct. Mater.* **2012**, *22*, 2310−2317.
(38) Lou, X. J. Polarization fatigue in ferroelectric thin films and related materials. *J. Appl. Phys.* **2009**, *105*, 024101.
(39) Scott, J. F.; Dawber, M. Oxygen-vacancy ordering as a fatigue mechanism in perovskite ferroelectrics. *Appl. Phys. Lett.* **2000**, *76*, 3801−3803.
(40) Chen, A.; Zhang, W.; Dedon, L. R.; Chen, D.; Khatkhatay, F.; MacManus-Driscoll, J. L.; Wang, H.; Yarotski, D.; Chen, J.; Gao, X.; et al. Couplings of Polarization with Interfacial Deep Trap and Schottky Interface Controlled Ferroelectric Memristive Switching. *Adv. Funct. Mater.* **2020**, *30*, 2000664.
(41) Yao, Z. H.; Song, Z.; Hao, H.; Yu, Z. Y.; Cao, M. H.; Zhang, S. J.; Lanagan, M. T.; Liu, H. X. Homogeneous/Inhomogeneous-Structured Dielectrics and their Energy-Storage Performances. *Adv. Mater.* **2017**, *29*, 1601727.

Recommended by ACS

Possible Extrinsic Ferroelectric-like Signals Originated from the Oxygen Vacancy Drift in HfO_2-Based Films
Yong Cheng, Zhigang Yin, *et al.*
APRIL 21, 2023
ACS APPLIED ELECTRONIC MATERIALS
READ

Origin of the Critical Thickness in Improper Ferroelectric Thin Films
Alexander Vogel, Marta D. Rossell, *et al.*
MARCH 30, 2023
ACS APPLIED MATERIALS & INTERFACES
READ

Ferroelectric Electroresistance after a Breakdown in Epitaxial $Hf_{0.5}Zr_{0.5}O_2$ Tunnel Junctions
Xiao Long, Josep Fontcuberta, *et al.*
JANUARY 30, 2023
ACS APPLIED ELECTRONIC MATERIALS
READ

Imaging Ferroelectric Nanodomains in Strained $BiFeO_3$ Nanoscale Films Using Scanning Low-Energy Electron Microscopy: Implications for Low-Power Devices
Haili Ma, Deyang Chen, *et al.*
APRIL 02, 2021
ACS APPLIED NANO MATERIALS
READ

Get More Suggestions >

https://doi.org/10.1021/acs.nanolett.3c00277
Nano Lett. 2023, 23, 4807−4814